

Tailoring Disordered/Ordered Phases to Revisit the Degradation Mechanism of High-Voltage $\text{LiNi}_{0.5}\text{Mn}_{1.5}\text{O}_4$ Spinel Cathode Materials

Huabin Sun, Anyang Hu, Stephanie Spence, Chunguang Kuai, Dong Hou, Linqin Mu, Jue Liu, Luxi Li, Chengjun Sun, Sami Sainio, Dennis Nordlund, Wei Luo, Yunhui Huang, and Feng Lin*


In the spinel oxide cathode family, $\text{LiNi}_{0.5}\text{Mn}_{1.5}\text{O}_4$ (LNMO) shows a high operating voltage (≈ 4.7 V vs Li/Li⁺) and excellent Li-ion mobility with stable 3D conducting channels. Ni/Mn cation disordered and ordered phases usually coexist in LNMO materials, and they have distinct structural and electrochemical properties, resulting in different battery performances for LNMO materials with different phase compositions. Identifying the correlation between phase compositions and electrochemical properties is of significance to the improvement of battery performance and understanding of degradation mechanisms. Herein, the disordered/ordered phase compositions in LNMO materials are tailored by post-annealing strategies and their impacts on electrochemical performance and degradation mechanisms from the surface to the bulk are systematically investigated. The ordered phase increases rapidly as Mn³⁺ is oxidized to Mn⁴⁺ through a post-annealing process. LNMO with an intermediate fraction of disordered and ordered phases gives rise to improved cycling stability. This article further reports that a high ordered phase fraction can preferentially protect Ni from dissolution during cycling. However, these results suggest that the transition metal dissolution and surface structural change of LNMO do not exhibit a direct correlation with cycling stability. These results indicate the capacity fading mainly correlates with the bulk structural distortion, leading to decreased Li-ion kinetics.

1. Introduction

Li-ion batteries are the dominant energy storage of choice for portable electronic devices due to their good performance, including high energy density and long-term cycle life. Li-ion batteries are increasingly used in electric vehicles (EVs), as they hold many advantages that other batteries cannot claim.^[1] At present, the range and charging time anxiety surrounding EVs have posed a great challenge to the development of high-energy batteries. The key to achieving higher energy density lies mainly in increasing the capacity or raising the operating voltage of cathode materials. In the past decade, extensive efforts have been made to pursue cathode materials with improved capacities, such as nickel-rich layered oxides,^[2] lithium/manganese-rich oxides,^[3] and disordered rock-salt oxides.^[4] Another strategy comes from the possibility of taking advantage of high-voltage spinel materials.^[5] Among them, the spinel $\text{LiNi}_{0.5}\text{Mn}_{1.5}\text{O}_4$ (LNMO)^[6] cathode is one of the most promising

H. Sun, A. Hu, S. Spence, C. Kuai, D. Hou, L. Mu, F. Lin
Department of Chemistry
Virginia Tech
Blacksburg, VA 24061, USA
E-mail: fenglin@vt.edu

H. Sun, W. Luo, Y. Huang
Institute of New Energy for Vehicles
School of Materials Science and Engineering
Tongji University
Shanghai 201804, China

 The ORCID identification number(s) for the author(s) of this article can be found under <https://doi.org/10.1002/adfm.202112279>.

© 2022 The Authors. Advanced Functional Materials published by Wiley-VCH GmbH. This is an open access article under the terms of the Creative Commons Attribution-NonCommercial License, which permits use, distribution and reproduction in any medium, provided the original work is properly cited and is not used for commercial purposes.

DOI: 10.1002/adfm.202112279

J. Liu
Neutron Scattering Division
Oak Ridge National Laboratory
Oak Ridge, TN 37831, USA

L. Li, C. Sun
Advanced Photon Source
Argonne National Laboratory
Argonne, IL 60439, USA

S. Sainio, D. Nordlund
Stanford Synchrotron Radiation Lightsource
SLAC National Accelerator Laboratory
Menlo Park, CA 94025, USA

S. Sainio
Microelectronics Research Unit
Faculty of Information Technology and Electrical Engineering
University of Oulu
P.O. Box. 4500, Oulu 90570, Finland

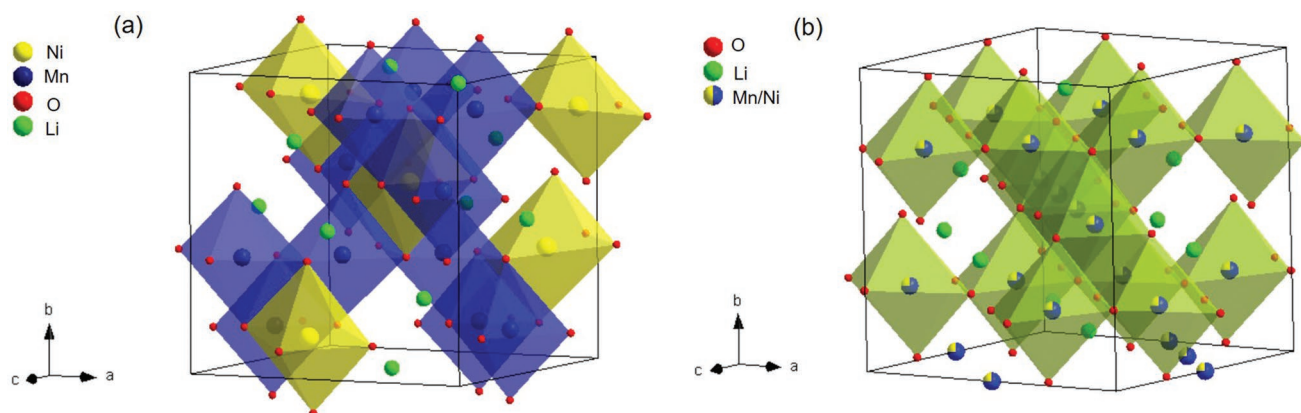


Figure 1. Schematic illustration of crystal structure for a) ordered ($P4_32$) and b) disordered ($Fd\bar{3}m$) LNMO.

candidates with a high operating voltage of ≈ 4.7 V versus Li/Li⁺ and a theoretical capacity of 147 mAh g⁻¹ (equivalent to a material level specific energy of ≈ 700 Wh kg⁻¹). Meanwhile, LNMO has fast 3D Li ion diffusion paths within the cubic lattice,^[6a,7] which makes LNMO a fast-charging capable cathode.

There are two different LNMO crystal structures depending on the distribution of Ni and Mn (**Figure 1**).^[8] The ordered structure, namely stoichiometric material, has a space group of $P4_32$, where Ni and Mn occupy the 4a and 12d octahedral sites with oxidation states of Ni²⁺ and Mn⁴⁺, respectively.^[8] Li extraction from the ordered structure leads to the oxidation of Ni²⁺ to Ni⁴⁺, whereas the Mn⁴⁺ remains inactive. The disordered structure has a space group of $Fd\bar{3}m$ in which Ni and Mn atoms are randomly distributed in the octahedral 16d sites.^[9] Most LNMO materials are non-stoichiometric with the presence of Mn³⁺, oxygen vacancies, and impurities.^[9] These two distinct LNMO crystal structures lead to differences in material properties and electrochemical performance. In most LNMO materials, the disordered/ordered phases usually co-exist, and thus it is hard to differentiate the exact contributions of disordered and ordered phases in the overall battery performance. Nevertheless, the large body of studies in the literature allows us to conclude that electrochemical performance is strongly correlated to the disordered/ordered phase ratio of LNMO materials.

Some studies reported that the disordered structure offers better electrochemical performance than the ordered counterpart due to two mechanisms: The presence of Mn³⁺ increases the electronic conductivity of the disordered structure, and the Li reaction mechanism resembles solid-solution reactions in the disordered structure.^[10] Xiao and co-workers reported that the Mn³⁺ formation in LNMO promotes Ni-Mn site disorder that is shown to facilitate the Li ion transport, especially at the high C-rate.^[11] When incorporated in a thin-film battery, the disordered LNMO showed even more impressive cycling performance. At 5 C, the capacity retentions for disordered LNMO and ordered LNMO are 95% and 48% after 2000 cycles, respectively.^[12] However, some other studies found that the ordered structure with a clear two-phase reaction behavior also shows excellent high rate capability and cycle life.^[13] The presence of Mn³⁺, however, may also induce Jahn–Teller distortion and metal dissolution via the disproportionation reaction ($2\text{Mn}^{3+} \rightarrow \text{Mn}^{2+} + \text{Mn}^{4+}$), which is detrimental to the electrochemical

performance of spinel cathodes (like, LNMO and LiMn₂O₄) in liquid electrolytes.^[14] In general, the disordered/ordered phase ratio is associated with Mn³⁺ and oxygen vacancies, which depends on the synthesis condition, especially the annealing process. For instance, Kim et al. reported the disordered LNMO ($Fd\bar{3}m$) structure could be transformed into the ordered structure ($P4_32$) by additional heating at 700 °C in the air.^[8] When annealed in an O₂ atmosphere, LNMO has a space group of $P4_32$ instead of $Fd\bar{3}m$.^[15] Post-annealing and annealing atmospheres can be used to tailor the disorder-to-order transition. To date, it remains a challenge to pinpoint the relationship between synthesis, structure, and performance.^[9,11,16] In particular, it is still unclear how the phase composition influences the degradation mechanism of LNMO materials during electrochemical cycling.

Herein, we apply a post-annealing strategy to tailor and optimize concentrations of disordered/ordered phases and Mn³⁺ content in LNMO materials, without influencing particle size and morphology. Our synchrotron, neutron, and electrochemical analyses show that an appropriately engineered disordered/ordered phase ratio can enhance the cycle life of LNMO cathodes. After post-annealing in air, the LNMO material consists of 52.1% disordered and 47.9% ordered structures. This phase composition gives rise to better battery performance than other compositions that have either higher or lower ordered phase concentrations. Soft X-ray absorption spectroscopy (sXAS) and X-ray fluorescence microscopy (XFM) results indicate that increasing the concentration of the ordered LNMO phase preferentially protects Ni from dissolution. Our further study indicates that capacity fading mainly correlates with the bulk structural distortion and shows a minor correlation with the surface processes or transition metal (TM) dissolution.

2. Results and Discussions

2.1. Characterizations of Pristine LNMO Materials

To tailor the disordered/ordered phase ratio of LNMO, we re-annealed LNMO materials under air or oxygen atmosphere at high-temperature and labeled them as LNMO-Air and LNMO-O₂. The X-ray diffraction (XRD) patterns for pristine and

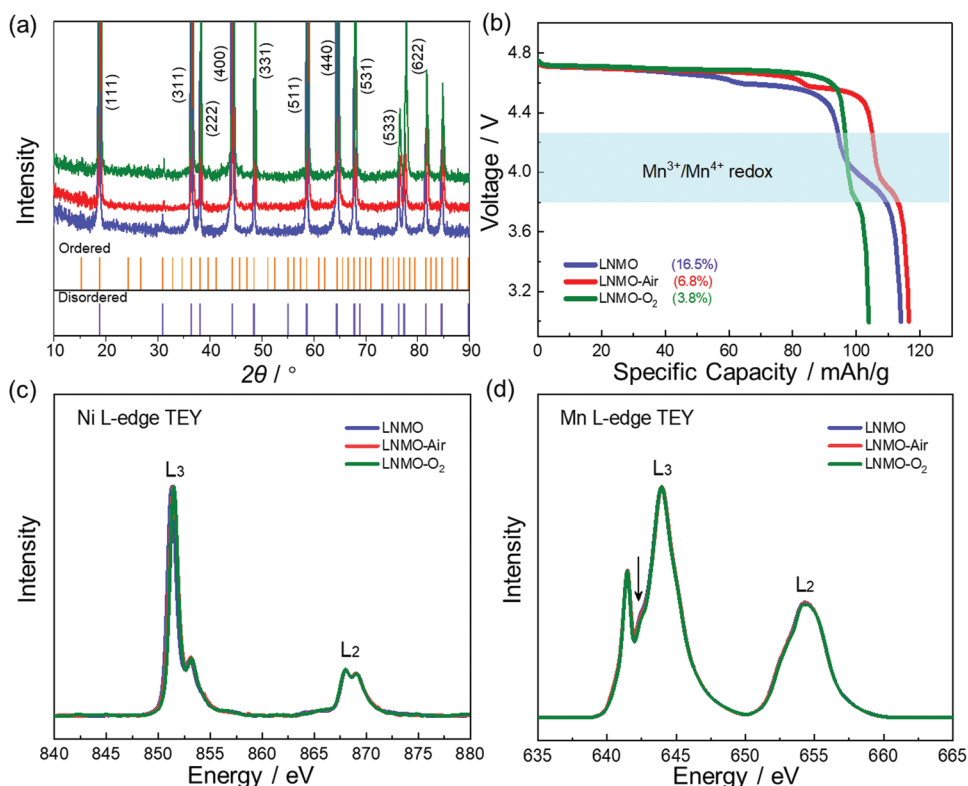


Figure 2. a) XRD patterns of $\text{LiNi}_{0.5}\text{Mn}_{1.5}\text{O}_4$ and post-annealed $\text{LiNi}_{0.5}\text{Mn}_{1.5}\text{O}_4$ in air and oxygen. The blue, red, and green curves correspond to LNMO, LNMO-Air, and LNMO- O_2 , respectively. The standard XRD peak positions for disordered and ordered $\text{LiNi}_{0.5}\text{Mn}_{1.5}\text{O}_4$ are placed at the bottom for comparison. b) The first discharge profiles of LNMO, LNMO-Air, and LNMO- O_2 at 0.5 C to illustrate the capacity contribution in the 3.80–4.25 V region due to the $\text{Mn}^{3+}/\text{Mn}^{4+}$ redox. Soft XAS spectra for c) Ni L-edge spectra and d) Mn L-edge spectra in the TEY mode of LNMO, LNMO-Air, and LNMO- O_2 electrodes before cycling.

post-annealed LNMO powders are displayed in **Figure 2a**. All diffraction peaks of three XRD patterns can be indexed into the structures of spinel $\text{LiNi}_{0.5}\text{Mn}_{1.5}\text{O}_4$. However, it is hard to distinguish disordered and ordered phases only based on XRD measurements due to the similarity of peak position and intensity between two phases by referring to the standard XRD peak positions. From the enlarged region of XRD patterns in Figure S1, Supporting Information, the peaks at $\approx 36.5^\circ$ and $\approx 38.2^\circ$ are shifted to higher angles for LNMO-Air and LNMO- O_2 samples, meaning a decrease of lattice parameter after post-annealing. The decrease of lattice parameter may be associated with the smaller Mn^{4+} ionic radius (0.530 Å) than Mn^{3+} ions (0.645 Å), suggesting an increase of Mn^{4+} ions after post-annealing. Redox reactions in LNMO provide information about the concentration of Mn^{3+} throughout the particle, which is usually done by quantifying the capacity contribution of the $\text{Mn}^{3+}/\text{Mn}^{4+}$ redox around the 4 V plateau.^[8] Here, we calculate the $\text{Mn}^{3+}/\text{Mn}^{4+}$ contribution between 3.80 and 4.25 V in the first discharge profile at 0.5 C (Figure 2b). We observe that the $\text{Mn}^{3+}/\text{Mn}^{4+}$ contribution to the total capacity has decreased substantially from 16.5% (LNMO) to 6.8% (LNMO-Air) and 3.8% (LNMO- O_2). Since the electrochemical quantification of Mn^{3+} is a bulk measurement, we believe that our quantitative results provide a good estimate for the Mn^{3+} concentration in the bulk. However, the Mn chemical state at the surface is not available through electrochemistry.

To directly characterize the effect of post-annealing on the electronic structure of transition metals and oxygen states at the particle surface, synchrotron sXAS was performed on electrodes before cycling. The measurement was in the total electron yield (TEY) mode with a depth sensitivity of <10 nm.^[17] The Ni L-edge spectra show no change for all of the three samples (Figure 2c), indicating that all these materials have Ni in the expected Ni^{2+} oxidation state despite the post-annealing. Mn L-edge spectra show that the Mn oxidation state is mostly at the Mn^{4+} oxidation state (Figure 2d). There is a small feature near the valley (labeled by the arrow) indicating a trace amount of Mn^{3+} at the surface for all three samples. Similarly, the Ni L-edge spectra and Mn L-edge in the FY mode show Ni in Ni^{2+} oxidation state and Mn in mostly Mn^{4+} oxidation state in Figure S2, Supporting Information. The depth sensitivity of fluorescence yield (FY) mode can be up to 50–100 nm, which is still considered subsurface for large particles in this case. Therefore, we conclude that the post-annealing does not alter the oxidation states of transition metals at the surface. Next, we performed Raman spectroscopy and neutron diffraction to investigate the disorder-to-order transition in the post-annealing.

Because of the similar X-ray scattering factors of Ni and Mn, XRD is unable to discriminate the disordered $\text{Fd}\bar{3}m$ and ordered P4_32 phases, especially when the ordered phase is minor.^[8] Raman spectroscopy as a local probe analysis method is sensitive enough to the crystal symmetry, which allows for

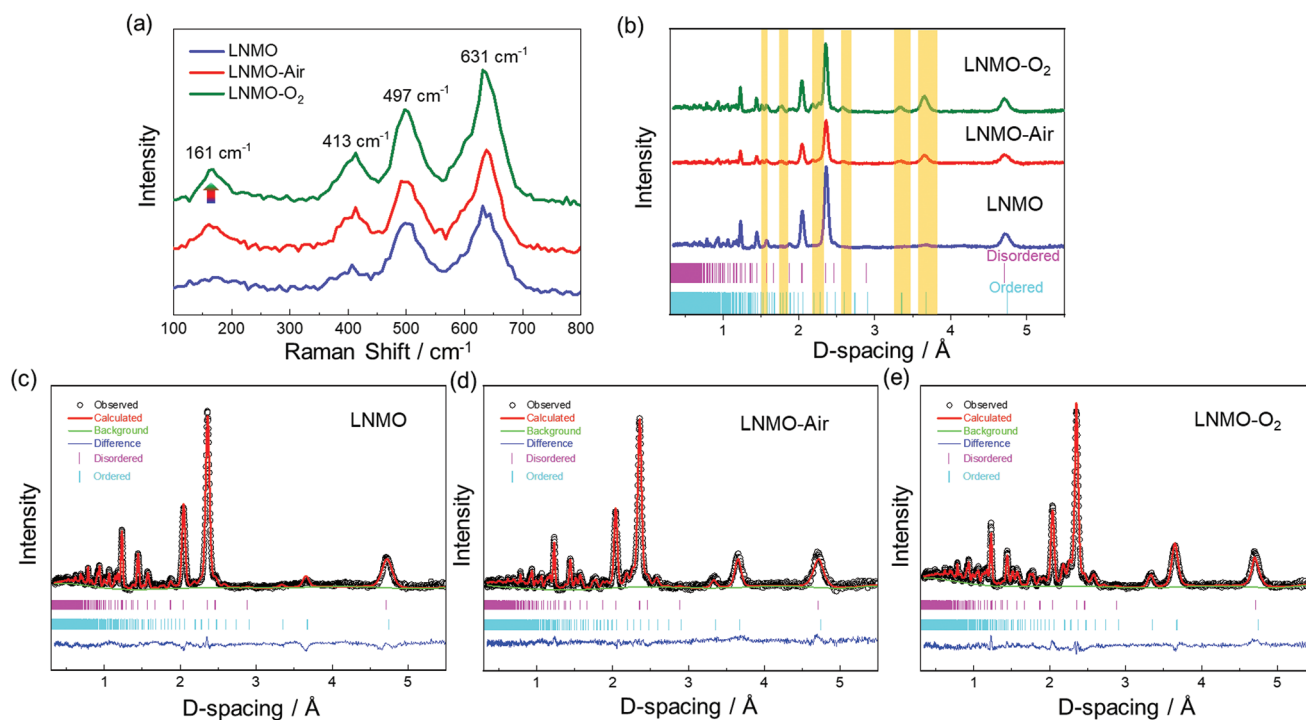


Figure 3. a) Raman spectra and b) neutron diffraction patterns for LNMO, LNMO-Air, and LNMO-O₂ powder. Representative reflections associated with the ordered phase are highlighted in orange. The corresponding Rietveld refinements of neutron diffraction pattern for c) LNMO, d) LNMO-Air, and e) LNMO-O₂. Bragg positions corresponding to the ordered spinel (P4₃32) and disordered spinel (Fd $\bar{3}$ m) are provided as references.

distinguishing between the disordered and ordered phases in LNMO.^[18] Figure 3a shows the Raman spectra of LNMO, LNMO-Air, and LNMO-O₂ samples. The peak around 631 cm⁻¹ is assigned to the symmetric Mn-O stretching vibration of the MnO₆ octahedra, and the peaks around 413 and 497 cm⁻¹ are assigned to the Ni²⁺-O stretching mode in the structure.^[18] The Raman spectra of the LNMO-Air and LNMO-O₂ samples exhibit higher intensities at 161 cm⁻¹, indicating the presence of higher concentrations of the ordered P4₃32 structure in these samples.^[19] The results indicate that the post-annealing can introduce the disorder-to-order transition in LNMO, whereas the disordered phase is dominant in the pristine LNMO sample.

The effect of post-annealing on the bulk crystal structure of the LNMO is then investigated by neutron diffraction and Rietveld refinement. Figure 3b compares the powder neutron diffraction patterns for LNMO, LNMO-Air, and LNMO-O₂ samples. As highlighted in orange, the characteristic reflections belonging to the ordered spinel phase appear in LNMO-Air and LNMO-O₂.^[20] The intensity of these peaks is stronger when the LNMO is post-annealed in oxygen than that in air. We then perform the Rietveld refinement based on the two-phase

model using the GSAS software. The results of the refinements were summarized in Figure 3c–e and Table 1. The pristine LNMO sample consisted of 79.6% of disordered LNMO (Fd $\bar{3}$ m) and 20.4% of ordered LNMO (P4₃32). After post-annealing, the LNMO samples showed a trend of decreasing amount of the disordered phase and simultaneously an increase of the ordered phase. The fraction of the ordered phase increases from 20.4% (for LNMO) to 47.9% (for LNMO-Air) and 85.8% (LNMO-O₂), showing that the post-annealing favors Ni/Mn cation ordering. Meanwhile, the lattice parameters of both disordered and ordered phases decrease after post-annealing, which is consistent with the XRD analysis discussed above. For the disordered and ordered phase distribution in LNMO, our recent work reported that phase heterogeneities exist in individual particles, with the presence of lattice variations and structural defects measured by synchrotron X-ray nano-diffraction.^[21] Combining with the electrochemical measurements, we conjecture that the bulk disorder-to-order transition is correlated with the bulk oxidation of Mn³⁺ to Mn⁴⁺ in Figure S3, Supporting Information, during the post-annealing. The morphology and surface area can influence the battery performance

Table 1. Summary of the neutron diffraction refinements for all three samples.

Sample	Composition		Lattice parameter [Å]		<i>R</i> _{wp}
	Disordered	Ordered	Disordered	Ordered	
LNMO	79.6%	20.4%	8.183(8)	8.173(1)	4.85%
LNMO-Air	52.1%	47.9%	8.163(4)	8.169(4)	4.82%
LNMO-O ₂	14.2%	85.8%	8.129(9)	8.159(6)	5.74%

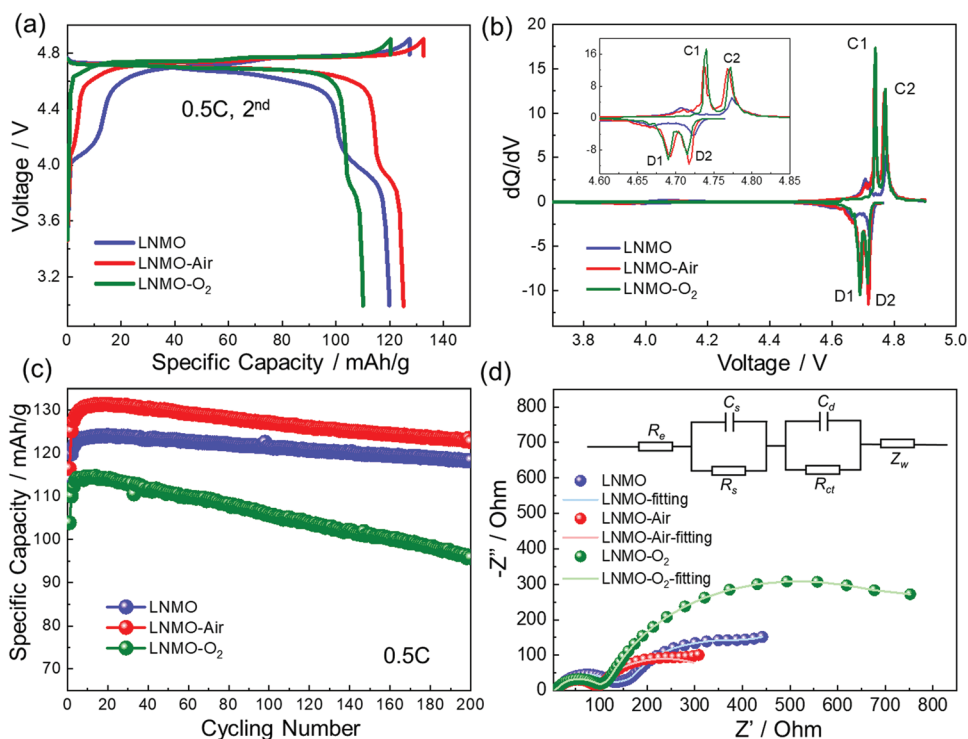


Figure 4. a) The second charge/discharge profiles at 22 °C between 3.0 and 4.9 V at 0.5 C ($1\text{ C} = 147\text{ mAh g}^{-1}$). b) dQ/dV plots based on second charge/discharge curves at 0.5 C and inset shows the region between 4.60 and 4.85 V. c) Cycling performance of LNMO, LNMO-Air, and LNMO-O₂ cathodes at 0.5 C at a voltage range 3.0–4.9 V, and d) Nyquist plot of EIS performed with fully discharged cells at 0.5 C after ten cycles of LNMO, LNMO-Air, and LNMO-O₂ cathodes. The inset equivalent circuit is used for EIS fitting.

of LNMO spinel oxides as well.^[22] LNMO, LNMO-Air, and LNMO-O₂ show no discernible difference in the particle size or morphology here (Figure S4, Supporting Information). Therefore, our current material system provides a good platform to investigate the relationship between synthesis, Mn³⁺ content, disordered/ordered phase ratio, and battery performance.

2.2. Electrochemical Performance of LNMO Cathodes

The electrochemical properties of LNMO, LNMO-Air, and LNMO-O₂ are examined in Li metal cells. The galvanostatic charge–discharge profiles were conducted between 3.0 and 4.9 V at 0.5 C (Figure 4a). All the cathodes exhibit two plateaus at approximately 4.0 and 4.7 V versus Li/Li⁺, which could be attributed to the redox reaction of Mn³⁺/Mn⁴⁺ and Ni²⁺/Ni⁴⁺ couples. The charge plateau around 4.7 V splits into two plateaus corresponding to Ni^{4+/3+} and Ni^{3+/2+} couples, and the extent of splitting is gradually decreased after post-annealing at 700 °C for LNMO-Air and LNMO-O₂ samples. The narrower separation between the two voltage plateaus indicates a higher degree of cation ordering.^[13b] A more detailed analysis is performed using the dQ/dV versus V plots in Figure 4b. The two dQ/dV peaks around 4.7 V indicate the two-step oxidation or reduction for the Ni²⁺/Ni⁴⁺ redox couple. The separation between these two peaks is indicative of the disordered/ordered phases, where a separation >50 mV is considered predominantly disordered and a separation of <30 mV is considered

predominantly ordered for spinel LNMO.^[9] The voltage gap between the two split peaks (C1 and C2) is 66 mV, 32 mV, and 32 mV during the oxidation process for LNMO, LNMO-Air and LNMO-O₂, indicating an increase in the ordered phase after the post-annealing. The long-term cycling performance of LNMO, LNMO-Air, and LNMO-O₂ at 0.5 C is presented in Figure 4c. The initial discharge capacities for LNMO, LNMO-Air, and LNMO-O₂ are approximately 114, 117, and 104 mAh g⁻¹, respectively. The LNMO-Air shows excellent cycling stability and retained 93.9% of its highest discharge capacity (10th cycle) after 200 cycles at 0.5 C, whereas the capacity retention of LNMO-O₂ is 83.5%, which may be due to the sluggish kinetics with increasing ordered phases.^[11]

In order to study the effect of the post-annealing on Li-ion kinetics, we perform electrochemical impedance spectroscopy (EIS). Figure 4d displays the Nyquist plots of the spinel electrodes after ten cycles. All EIS spectra contain two semicircles in the high- and medium-frequency regions, which are usually assigned to cathode electrolyte interphase film resistance and charge transfer impedance at the electrode surface.^[23] The EIS was simulated by the Zview software using the equivalent circuit shown in the inset of Figure 4d. R_e is the bulk resistance of the cell, R_s is the surface film resistance, R_{ct} is the charge-transfer resistance, C_s is the surface film capacitance, C_d is the double-layer capacitance, and Z_w is the Warburg impedance. The results of EIS fitting are summarized in Table S1, Supporting Information. The R_s and R_{ct} of the LNMO-Air sample are found to be smaller than those of the LNMO and

LNMO-O₂ samples, indicating that LNMO-Air has better ionic conductivity and lower electrochemical polarization with better electrochemical performance. Interestingly, though LNMO exhibits a higher degree of disordered phase than LNMO-Air, it exhibits lower Li ion kinetics, implying that the degree of cation ordering in 16d octahedral sites is not the only factor for the Li⁺ transport in LNMO spinels.

2.3. Degradation Mechanism during Cycling

Many cathode studies have investigated the relationship between surface chemistry and performance stability.^[24] The undesired side reactions with electrolyte, including TM dissolution, may initiate at the particle surface, leading to structure reconstruction and impedance development during cycling. It is not always trivial to establish such a relationship, especially for electrodes after long-term cycles. Part of the challenge is due to the significant redeposition of TM cations onto the cathode surface. These redeposited TMs are usually in their lower oxidation states. Therefore, spectroscopically, it becomes challenging to pinpoint the origin of the surface TM reduction, either from TM reduction in the cathode lattice or from the redeposited TM-organic complex. We believe it is important to supplement the characterization of surface TM oxidation states with TM dissolution studies.

The electrochemical performance of LNMO was reported to be highly correlated to TM dissolution, especially Mn, which

has been studied by simulations and experiments.^[25] Mn dissolution during cycling significantly reduces the cycle life of LNMO with continuous Li loss and surface impedance rise.^[26] The Mn dissolution is highly related to the protonation of surface oxygen atoms upon delithiation and side reactions between surface Mn and electrolytes.^[27] Many studies have reported that Mn gets dissolved in the electrolyte as Mn²⁺-containing species, which can be generated from the Mn³⁺ disproportionation reaction.^[28] In addition, there is a significant degree of Mn reduction at the surface of LNMO upon charging to 4.9 V, suggesting that Mn²⁺ evolution is also dependent on the side reactions with the electrolyte during cycling.^[29] Therefore, we perform surface-sensitive sXAS in the TEY mode for LNMO, LNMO-Air, and LNMO-O₂ after 200 cycles to identify surface Mn oxidation state. In sXAS Mn L-edge spectra (Figure 5a), the peak intensity at 640 eV, assigned to Mn²⁺, gradually decreases with an increase of ordered phase in LNMO materials after 200 cycles. Overall, the intensity at the lower energy side of the L₃-edge increases from LNMO-O₂ to LNMO-Air and LNMO, showing the surface Mn experienced the most reduction in the LNMO sample. Such a Mn reduction trend does not follow the trend of cycling stability in Figure 4c. There is no discernible difference of Ni valence state in LNMO, LNMO-Air, and LNMO-O₂ after 200 cycles with negligible intensity ratio change of peak L_{3high}/L_{3low} (Figure 5b). In sXAS O K-edge spectra, the increase of the pre-edge peak intensity corresponds to increasing TM3d-O2p hybridization and also correlates with increasing TM oxidation states. The pre-edge peak intensity of LNMO-O₂ is larger

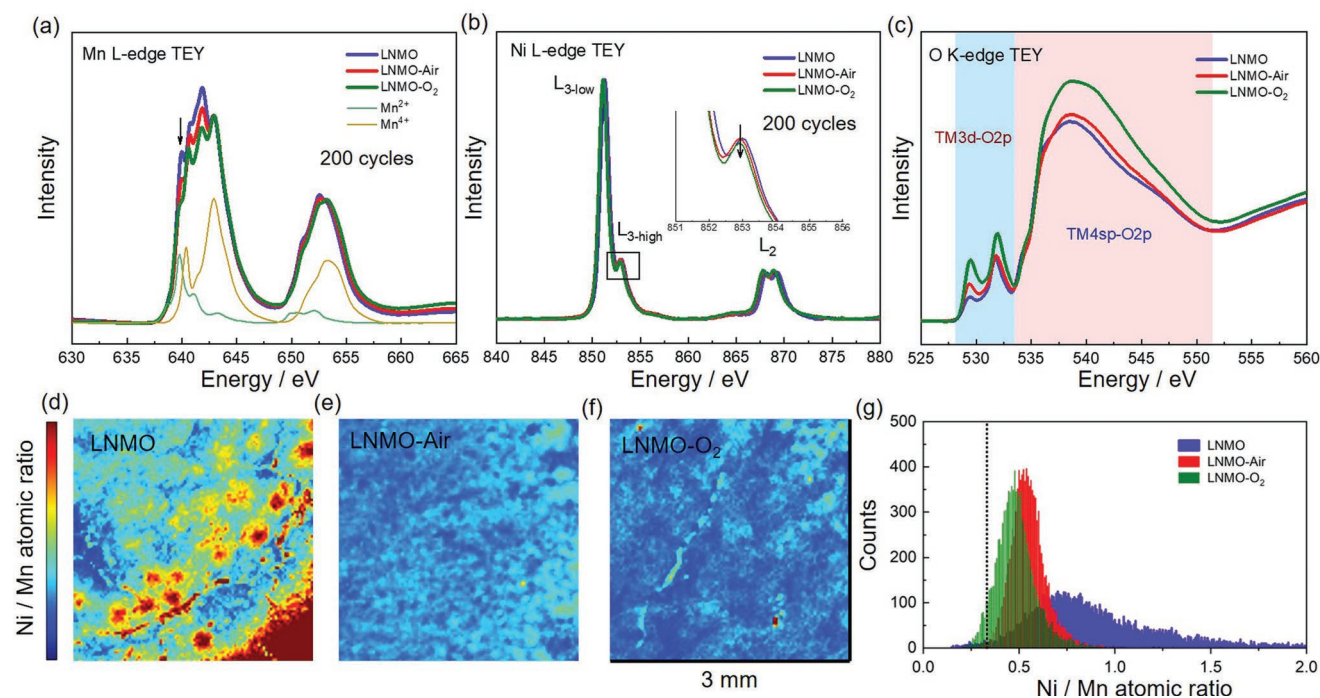


Figure 5. a) Mn L-edge, b) Ni L-edge, and c) O K-edge soft XAS/TEY spectra for LNMO, LNMO-Air, and LNMO-O₂ electrodes were collected fully discharged after 200 cycles at 0.5 C. In Mn L-edge spectra, Mn²⁺ and Mn⁴⁺ reference spectra are provided on the bottom. The peaks at 640 eV assigned by black arrow are feature peaks of Mn²⁺, which signify the degree of Mn reduction at the surface. Ni/Mn atomic ratio distribution mapping on Li metal anode surface after 200 cycles at 0.5 C with d) LNMO, e) LNMO-Air, and f) LNMO-O₂ cathodes and g) the corresponding histograms, which are based on the pixel-by-pixel quantification analysis of synchrotron X-ray fluorescence microscopy on the Li metal anodes paired with the spinel cathodes. The vertical dashed line represents the Ni/Mn atomic ratio (1/3) if Ni and Mn dissolution follows the Ni/Mn stoichiometry in LNMO.

than LNMO and LNMO-Air (Figure 5c), indicating a higher TM oxidation state in LNMO-O₂, which is consistent with the results in Figure 5a.

In summary, although it was found powerful in some studies that TM reduction is a good indicator for cycling stability, especially for layered cathodes, we show here that TM reduction has no clear relationship with cycling stability. We believe the dynamic TM dissolution and redeposition are responsible for complicating the analysis. We then performed XFM experiments to investigate the dissolution behavior of Ni and Mn by measuring the Ni and Mn deposited on the lithium metal anode surface. XFM is a highly sensitive technique with a sub-ppm detection limit and can cover tens of micrometers to a few millimeters in dimension. We found TM deposition is highly heterogeneous on the Li metal anode. To improve the statistical significance, we focus on investigating the relative dissolution of Ni and Mn (Figure 5d–g). These results allow us to make the following conclusion about TM dissolution: 1) In all three samples, the Ni/Mn ratio on the Li metal anode is higher than the Ni/Mn stoichiometric ratio in LNMO, indicating a preferential Ni dissolution over Mn dissolution; 2) increasing the fraction of ordered LNMO decreases the Ni/Mn ratio and makes the distribution less heterogeneous. Collectively, one can conclude that increasing the fraction of ordered LNMO can decrease Ni dissolution relative to Mn dissolution. However, there is still no direct correlation between TM dissolution and battery cycling performance, since the best performing LNMO-Air has the dissolution behavior in between LNMO and LNMO-O₂. In summary, the sXAS and XFM results show that neither TM dissolution nor the surface properties are the dominant factors governing the electrochemical degradation of LNMO cathodes in the present study.

Although surface chemistry plays a vital role in cathode's performance, the lithium delithiation/lithiation behaviors are ultimately an overall chemical process in cathode materials, including surface and bulk structures. The capacity degradation of LNMO is closely related to, but not limited to, the surface chemistry variation or structure reconstruction. In some cases, the battery performance, especially cycling stability, highly depends on bulk chemistry and structure evolution, such as the electronic structure of TM, crystallographic orientations, charge distribution, and chemomechanical properties.^[30] With respect to TM redox behaviors during cycling, it is strongly associated with their coordination environments or structural changes in the bulk. Hence, we performed X-ray absorption near-edge structure (XANES) analyses to elucidate the bulk chemistry and structure evolution of LNMO, LNMO-Air, and LNMO-O₂ cathodes upon cycling. The LNMO-Air appears to have the most stable Mn and Ni K-edge spectra after cycling for 200 cycles, which may be due to better bulk structure stability with higher Li-ion kinetics, thus leading to improvement of electrochemical performance (Figure 6a,b). Moreover, the Raman spectra show less variation and less peak broadening after 200 cycles for LNMO-Air than that for LNMO and LNMO-O₂ (Figure 6c). Combining with the micron-sized primary particles of LNMO in Figure S4, Supporting Information, we consider that the Raman results can be assigned to sub-surface, or even bulk, of LNMO particles here. Overall, the hard XAS and Raman characterizations suggest that the improved cycling performance

of the LNMO-Air sample is likely attributed to the more stable bulk electronic structure and less structural distortion.

3. Conclusion

The electrochemical performance of LNMO cathode is closely linked to their lattice structure, especially disordered/ordered phase ratio and Mn³⁺ content. Details of synthetic conditions affect Ni/Mn cation ordering, which in turn influences the electrochemical performance of LNMO. The tendency for the disordered phase to transform to the ordered phase closely correlates with the post-annealing atmosphere. Neutron diffraction results show that the ordered phase increases from 20.4% in pristine LNMO to 47.9% and 85.8% after post-annealing in air and oxygen, respectively. The increased structural ordering accompanies the decrease of Mn³⁺ content in the lattice. The LNMO-Air could deliver a discharge capacity of 131 mAh g⁻¹ at 0.5 C and the highest capacity retention of 93.9% after 200 cycles at 0.5 C. Mn and Ni dissolution takes place in all the samples studied. Increasing the ordered phase in LNMO can preferentially suppress Ni dissolution during cycling. Surface processes, such as TM reduction and dissolution, exhibit no clear relationship with the battery performance reported here. The characterization results appear to suggest that an intermediate disordered/ordered phase ratio can mitigate the structural distortion, thus offering the optimized electrochemical performance. Our study highlights the critical importance of a well-tailored phase ratio for stabilizing LNMO cathodes.

4. Experimental Section

Material Synthesis: The pristine spinel LiNi_{0.5}Mn_{1.5}O₄ powder was provided by the U.S. Department of Energy's (DOE) CAMP (Cell Analysis, Modeling, and Prototyping) Facility, Argonne National Laboratory. Then, LiNi_{0.5}Mn_{1.5}O₄ materials were post-annealed at 700 °C for 8 h under either air or oxygen atmosphere with a heating rate of 5 °C min⁻¹. For under air condition, the crucible with LNMO powder was placed into a tube furnace without gas flow to obtain air atmosphere. For under oxygen atmosphere, the pure oxygen was continuously flowed into the tube at a rate of 1.0 L min⁻¹ during overall annealing process. Then, the furnace with LNMO powder was cooled naturally to room temperature and denoted as LNMO-Air and LNMO-O₂. The LiNi_{0.5}Mn_{1.5}O₄ powder without the post-annealing is denoted as LNMO.

Characterization: XRD patterns were obtained from 10–90° with a step size of 0.02° at room temperature using a benchtop Rigaku Miniflex II with a Cu K_α radiation source (λ = 1.54 Å). Schematic diagrams of LNMO crystal structures were made by the Diamond Software. sXAS was performed on 31-pole wiggler beamline 10–1 at Stanford Synchrotron Radiation Lightsource. A ring current of 350 mA and a 1000 L mm⁻¹ spherical grating monochromator with a 20 μm entrance and exit slit were used to acquire ≈10¹¹ ph s⁻¹ at 0.28 eV resolution in a 1 mm² beam spot. Data was collected under ultrahigh vacuum (10⁻⁹ Torr) in a single load at room temperature. Spectra were normalized by the current from freshly evaporated gold on a fine grid positioned upstream from the main chamber. Raman spectra were collected on a WITec Raman spectrometer with a 633 nm laser beam. Time-of-flight powder neutron diffraction measurements were conducted at the POWGEN diffractometer (beamline 11A) at the Spallation Neutron Source at Oak Ridge National Laboratory.^[31] The LNMO powder samples were analyzed via the Rietveld method using the GSAS/EXPGUI package.^[32] Scanning electron microscopy (SEM) was used to investigate the particle

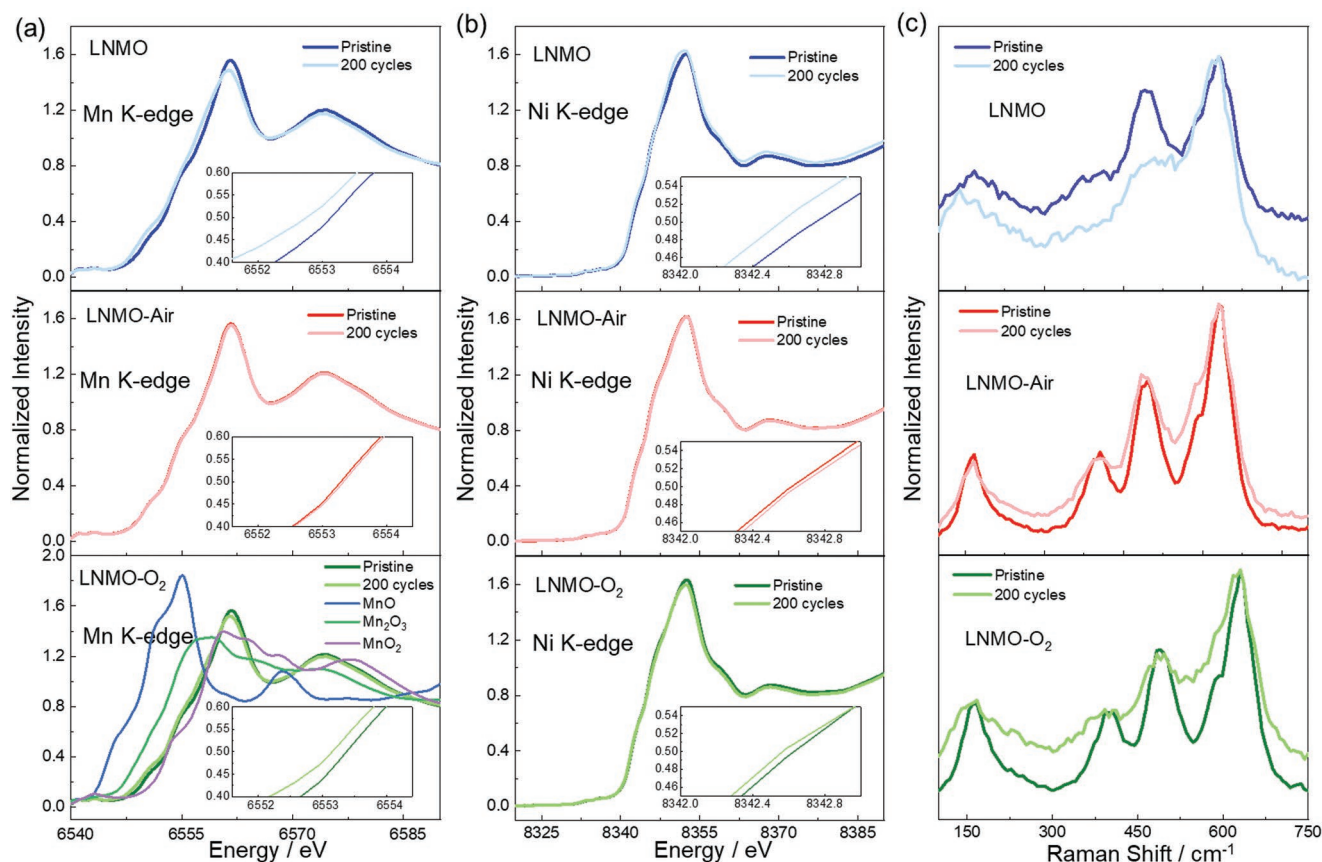


Figure 6. a) Mn K-edge XANES, b) Ni K-edge XANES, and c) Raman spectra of LNMO (blue), LNMO-Air (red), and LNMO-O₂ (green) electrodes at pristine state and after 200 cycles at 0.5 C. In Mn K-edge XANES spectra, MnO, Mn₂O₃, and MnO₂ are provided as references.

morphology using an LEO FESEM at an acceleration voltage of 5.0 kV. Hard XAS measurements were performed on the electrodes in the pristine state and after 200 cycles fully discharged in the transmission mode at the beamline 20-BM-B of the advanced photon source (APS) at Argonne National Laboratory. The incident beam was monochromatized by using a Si (111) fixed-exit and a double-crystal monochromator. All electrodes for hard XAS were sealed with Kapton tape in the glovebox filling with Ar atmosphere for measurement. Synchrotron XFM analyses were conducted at the 2-ID-E and 34-ID-E beamlines of the APS, Argonne National Laboratory. The samples were raster-scanned by a sub-micrometer (≈ 700 nm) focused 10 keV X-ray beam with a step size of 0.5 μm . The fluorescent X-rays were detected with a four-element silicon-drift Vortex detector. The Li metal anode samples for XFM measurements were prepared by sealing in Kapton tape.

Electrochemical Measurements: The LNMO electrodes were prepared by mixing LNMO active material, carbon black, and polyvinylidene fluoride binder (80:10:10 wt%) in N-methylpyrrolidone solvent. The slurries were cast on carbon-coated Al foils via the doctor blade method. Then, the coated electrode was cut into cathode disks and dried in a vacuum oven at 120 °C overnight before being transferred to an Ar-filled glovebox. The active mass loading was around 4.5 mg cm⁻². Thin electrodes were chosen to minimize the internal polarization-caused degradation, which allowed for studying material degradation within minimal influence from electrode factors. Coin cells (CR2032) were assembled with Li foils as the anode, glass fiber as the separator, and 1 M LiPF₆ in 3:7 vol% ethylene carbonate (EC)/dimethyl carbonate (DMC) as the electrolyte. All coin cells were cycled using a LAND battery testing system from 3.0 to 4.9 V versus Li/Li⁺. For galvanostatic charge/discharge experiments, cells were cycled at 0.5 C (1 C = 147 mA g⁻¹). The EIS was examined by applying an AC voltage of 5 mV over a frequency

range of 0.01 Hz to 100 kHz of coin cells at a fully discharged state at 0.5 C after ten cycles.

Supporting Information

Supporting Information is available from the Wiley Online Library or from the author.

Acknowledgements

The work at Virginia Tech was supported by Department of Chemistry startup funds. Use of the Stanford Synchrotron Radiation Lightsource, SLAC National Accelerator Laboratory, was supported by the U.S. Department of Energy, Office of Science, Office of Basic Energy Sciences under Contract No. DE-AC02-76SF00515. The pristine LNMO powder was produced at the U.S. Department of Energy's (DOE) CAMP (Cell Analysis, Modeling and Prototyping) Facility, Argonne National Laboratory. The CAMP Facility is fully supported by the DOE Vehicle Technologies Program (VTP) within the core funding of the Applied Battery Research (ABR) for Transportation Program. This research used resources of the Advanced Photon Sources at Argonne National Laboratory, which is a U.S. DOE Office of Science User Facility under contract No. DE-AC02-06CH11357. The use of the Spallation Neutron Source at Oak Ridge National Laboratory was supported by the U.S. DOE Office of Science, Office of Basic Energy Sciences under Contract No. DE-AC05-00OR22725. This research used resources of the Advanced Light Source at Lawrence Berkeley National Laboratory, which is a

U.S. DOE Office of Science User Facility under contract No. DE-AC02-05CH11231. The authors thank Dr. Gi-Hyeok Lee and Dr. Wanli Yang for fruitful discussion and soft XAS experiments. S.S. acknowledges funding from the Walter Ahlström Foundation. S.S. received funding from the European Union's Horizon 2020 research and innovation programme under the Marie Skłodowska-Curie grant agreement No 841621.

Conflict of Interest

The authors declare no conflict of interest.

Authors Contribution

F.L. conceived the study. H.S. and F.L. designed the experiments. A.H. performed XRD, SEM, and Raman measurements. J.L. performed neutron diffraction measurements. S.S. and D.N. collected soft XAS data. C.S. assisted with the hard XAS measurements. L.L. performed synchrotron XFM measurements. S.S., D. H., L.M., and C.K. assisted the data analysis. H.S. and F.L. wrote the manuscript with feedback from all coauthors. All authors have given approval to the final version of the manuscript.

Data Availability Statement

The data that support the findings of this study are available from the corresponding author upon reasonable request.

Keywords

cycle life, disorder-to-order transition, fading mechanism, metal dissolution, spinel cathodes

Received: December 1, 2021

Revised: January 27, 2022

Published online: February 26, 2022

- [1] M. Li, J. Lu, Z. Chen, K. Amine, *Adv. Mater.* **2018**, *30*, 1800561.
- [2] a) J. Xu, F. Lin, M. M. Doeff, W. Tong, *J. Mater. Chem. A* **2017**, *5*, 874; b) X. Zeng, C. Zhan, J. Lu, K. Amine, *Chem* **2018**, *4*, 690; c) J. Kim, H. Lee, H. Cha, M. Yoon, M. Park, J. Cho, *Adv. Energy Mater.* **2018**, *8*, 1702028; d) G. L. Xu, X. Liu, A. Daali, R. Amine, Z. Chen, K. Amine, *Adv. Funct. Mater.* **2020**, *30*, 2004748.
- [3] a) A. Manthiram, J. C. Knight, S. T. Myung, S. M. Oh, Y. K. Sun, *Adv. Energy Mater.* **2016**, *6*, 1501010; b) J. Song, B. Li, Y. Chen, Y. Zuo, F. Ning, H. Shang, G. Feng, N. Liu, C. Shen, X. Ai, D. Xia, *Adv. Mater.* **2020**, *32*, 2000190; c) D. Eum, B. Kim, S. J. Kim, H. Park, J. Wu, S.-P. Cho, G. Yoon, M. H. Lee, S. K. Jung, W. Yang, W. M. Seong, K. Ku, O. Tamwattana, S. K. Park, I. Hwang, K. Kang, *Nat. Mater.* **2020**, *19*, 419.
- [4] X. Zheng, Z. Xu, S. Li, Y. Zhang, J. Zhang, C. Kuai, L. Tao, M. M. Rahman, Y. Zhang, S.-J. Lee, C.-J. Sun, L. Li, W. Hu, D. Nordlund, J. Liu, Y. Liu, F. Lin, *Acta Mater.* **2021**, *212*, 116935.
- [5] W. Li, B. Song, A. Manthiram, *Chem. Soc. Rev.* **2017**, *46*, 3006.
- [6] a) Q. Zhong, A. Bonakdarpour, M. Zhang, Y. Gao, J. R. Dahn, *J. Electrochem. Soc.* **1997**, *144*, 205; b) P. V. Sushko, K. M. Rosso, J. G. Zhang, J. Liu, M. L. Sushko, *Adv. Funct. Mater.* **2013**, *23*, 5530.
- [7] a) B. Markovsky, Y. Talyosoff, G. Salitra, D. Aurbach, H. J. Kim, S. Choi, *Electrochem. Commun.* **2004**, *6*, 821; b) R. Santhanam, B. Rambabu, *J. Power Sources* **2010**, *195*, 5442.
- [8] J. H. Kim, S. T. Myung, C. S. Yoon, S. G. Kang, Y. K. Sun, *Chem. Mater.* **2004**, *16*, 906.
- [9] J. Cabana, M. Casas-Cabanas, F. O. Omenya, N. A. Chernova, D. Zeng, M. S. Whittingham, C. P. Grey, *Chem. Mater.* **2012**, *24*, 2952.
- [10] a) Y. F. Deng, S. X. Zhao, Y. H. Xu, K. Gao, C. W. Nan, *Chem. Mater.* **2015**, *27*, 7734; b) J. Liu, A. Huq, Z. Moorhead-Rosenberg, A. Manthiram, K. Page, *Chem. Mater.* **2016**, *28*, 6817.
- [11] J. Xiao, X. Chen, P. V. Sushko, M. L. Sushko, L. Kovarik, J. Feng, Z. Deng, J. Zheng, G. L. Graff, Z. Nie, D. Choi, J. Liu, J. G. Zhang, M. S. Whittingham, *Adv. Mater.* **2012**, *24*, 2109.
- [12] J. Li, Q. Zhang, X. Xiao, Y. T. Cheng, C. Liang, N. J. Dudney, *J. Am. Chem. Soc.* **2015**, *137*, 13732.
- [13] a) X. Ma, B. Kang, G. Ceder, *J. Electrochem. Soc.* **2010**, *157*, A925; b) D. W. Shin, C. A. Bridges, A. Huq, M. P. Paranthaman, A. Manthiram, *Chem. Mater.* **2012**, *24*, 3720; c) Z. M. Rosenberg, A. Huq, J. B. Goodenough, A. Manthiram, *Chem. Mater.* **2015**, *27*, 6934.
- [14] T. F. Yi, J. Mei, Y. R. Zhu, *J. Power Sources* **2016**, *316*, 85.
- [15] Y. Idemoto, H. Narai, N. Koura, *J. Power Sources* **2003**, *119–121*, 125.
- [16] L. Wang, H. Li, X. Huang, E. Baudrin, *Solid State Ionics* **2011**, *193*, 32.
- [17] F. Lin, Y. Liu, X. Yu, L. Cheng, A. Singer, O. G. Shpyrko, H. L. Xin, N. Tamura, C. Tian, T. C. Weng, X. Q. Yang, Y. S. Meng, D. Nordlund, W. Yang, M. M. Doeff, *Chem. Rev.* **2017**, *117*, 13123.
- [18] J. Song, D. W. Shin, Y. Lu, C. D. Amos, A. Manthiram, J. B. Goodenough, *Chem. Mater.* **2012**, *24*, 3101.
- [19] S. L. Spence, Z. Xu, S. Sainio, D. Nordlund, F. Lin, *Inorg. Chem.* **2020**, *59*, 10591.
- [20] J. H. Kim, A. Huq, M. Chi, N. P. W. Pieczonka, E. Lee, C. A. Bridges, M. M. Tessema, A. Manthiram, K. A. Persson, B. R. Powell, *Chem. Mater.* **2014**, *26*, 4377.
- [21] S. L. Spence, A. Hu, M. Jiang, Z. Xu, Z. Yang, M. M. Rahman, L. Li, Y. S. Chu, X. Xiao, X. Huang, F. Lin, *ACS Energy Lett.* **2022**, *7*, 690.
- [22] B. Hai, A. K. Shukla, H. Duncan, G. Chen, *J. Mater. Chem. A* **2013**, *1*, 759.
- [23] Y. F. Deng, S. X. Zhao, Y. H. Xu, C. W. Nan, *J. Mater. Chem. A* **2014**, *2*, 18889.
- [24] a) F. Lin, I. M. Markus, D. Nordlund, T. C. Weng, M. D. Asta, H. L. Xin, M. M. Doeff, *Nat. Commun.* **2014**, *5*, 3529; b) R. Lin, S. M. Bak, Y. Shin, R. Zhang, C. Wang, K. Kisslinger, M. Ge, X. Huang, Z. Shadik, A. Pattammattel, H. Yan, Y. Chu, J. Wu, W. Yang, M. S. Whittingham, H. L. Xin, X. Q. Yang, *Nat. Commun.* **2021**, *12*, 2350.
- [25] a) N. P. W. Pieczonka, Z. Liu, P. Lu, K. L. Olson, J. Moote, B. R. Powell, J. H. Kim, *J. Phys. Chem. C* **2013**, *117*, 15947; b) N. N. Intan, K. Klyukin, V. Alexandrov, *ACS Appl. Mater. Interfaces* **2019**, *11*, 20110.
- [26] Y. Chen, L. Ben, B. Chen, W. Zhao, X. Huang, *Adv. Mater. Interfaces* **2018**, *5*, 1800077.
- [27] a) Y. Shilina, B. Ziv, A. Meir, A. Banerjee, S. Ruthstein, S. Luski, D. Aurbach, I. C. Halalay, *Anal. Chem.* **2016**, *88*, 4440; b) A. Jarry, S. Gottis, Y. S. Yu, J. Roque Rosell, C. Kim, J. Cabana, J. Kerr, R. Kostecki, *J. Am. Chem. Soc.* **2015**, *137*, 3533.
- [28] a) J. C. Hunter, *J. Solid State Electrochem.* **1981**, *39*, 142; b) G. G. Amatucci, N. Pereira, T. Zheng, J. M. Tarascon, *J. Electrochem. Soc.* **2001**, *148*, A171; c) L. W. Ma, B. Z. Chen, X. C. Shi, W. Zhang, K. Zhang, *Colloids Surf. A Physicochem. Eng.* **2010**, *369*, 88.
- [29] R. Qiao, Y. Wang, P. Olalde Velasco, H. Li, Y. S. Hu, W. Yang, *J. Power Sources* **2015**, *273*, 1120.
- [30] a) D. Kim, J. M. Lim, Y. G. Lim, J. S. Yu, M. S. Park, M. Cho, K. Cho, *Chem. Mater.* **2015**, *27*, 6450; b) L. Mu, R. Lin, R. Xu, L. Han, S. Xia, D. Sokaras, J. D. Steiner, T.-C. Weng, D. Nordlund,

- M. M. Doeff, Y. Liu, K. Zhao, H. L. Xin, F. Lin, *Nano Lett.* **2018**, *18*, 3241; c) Z. Xu, Z. Jiang, C. Kuai, R. Xu, C. Qin, Y. Zhang, M. M. Rahman, C. Wei, D. Nordlund, C. J. Sun, X. Xiao, X. W. Du, K. Zhao, P. Yan, Y. Liu, F. Lin, *Nat. Commun.* **2020**, *11*, 83; d) S. Li, Z. Jiang, J. Han, Z. Xu, C. Wang, H. Huang, C. Yu, S. J. Lee, P. Pianetta, H. Ohldag, J. Qiu, J. S. Lee, F. Lin, K. Zhao, Y. Liu, *Nat. Commun.* **2020**, *11*, 4433.
- [31] J. Neufeind, M. Feygenson, J. Carruth, R. Hoffmann, K. K. Chipley, *Nucl. Instrum. Methods Phys. Res. B* **2012**, *287*, 68.
- [32] B. Toby, *J. Appl. Crystallogr.* **2001**, *34*, 210.